

**MODELLING AND LABORATORY TESTING OF PARTICLE RESUSPENSION AND TRANSPORT FOR
THE ASSESSMENT OF TERRESTRIAL-BORNE BIOLOGICAL CONTAMINATION OF THE
SAMPLES ON THE MARS 2020 MISSION**

Ioannis Mikellides⁽¹⁾, Nicole Chen⁽²⁾, Stephen Liao⁽³⁾, Evan Droz⁽⁴⁾, Zachary Strimbu⁽⁵⁾, Moogega Stricker⁽⁶⁾, Fei Chen⁽⁷⁾, Ganesh Babu Malli Mohan⁽⁸⁾, Jerami Mennella⁽⁹⁾, Parthiv Shah⁽¹⁰⁾, Albert Robinson⁽¹¹⁾, Douglas Bernard⁽¹²⁾ and Adam Steltzner⁽¹³⁾

⁽¹⁾Jet Propulsion Laboratory, California Institute of Technology, Pasadena, CA, 91109, USA. M/S 125-109.
Ioannis.G.Mikellides@jpl.nasa.gov

⁽³⁾Jet Propulsion Laboratory, California Institute of Technology, Pasadena, CA, 91109, USA. M/S 125-123.
Nicole.C.Chen@jpl.nasa.gov

⁽²⁾Jet Propulsion Laboratory, California Institute of Technology, Pasadena, CA, 91109, USA. M/S 125-211.
Stephen.Liao@jpl.nasa.gov

⁽⁴⁾Jet Propulsion Laboratory, California Institute of Technology, Pasadena, CA, 91109, USA. M/S 157-316.
Evan.A.Droz@jpl.nasa.gov

⁽⁵⁾Ohio State University, Columbus, OH, 43210, USA. *strimbu.3@buckeyemail.osu.edu*

⁽⁶⁾Jet Propulsion Laboratory, California Institute of Technology, Pasadena, CA, 91109, USA. M/S 321-400.
Moogega.Cooper@jpl.nasa.gov

⁽⁷⁾Jet Propulsion Laboratory, California Institute of Technology, Pasadena, CA, 91109, USA. M/S 89.
fei.chen@jpl.nasa.gov

⁽⁸⁾Jet Propulsion Laboratory, California Institute of Technology, Pasadena, CA, 91109, USA. M/S 89.
Ganesh.Babu.Malli.Mohan@jpl.nasa.gov

⁽⁹⁾Jet Propulsion Laboratory, California Institute of Technology, Pasadena, CA, 91109, USA. M/S 89.
jerami.mennella@jpl.nasa.gov

⁽¹⁰⁾ATA Engineering, Inc., San Diego, CA, 92128. *parthiv.shah@ata-e.com*

⁽¹¹⁾ATA Engineering, Inc., San Diego, CA, 92128. *albert.robinson@ata-e.com*

⁽¹²⁾Jet Propulsion Laboratory, California Institute of Technology, Pasadena, CA, 91109, USA. M/S 321-400.
douglas.e.bernard@jpl.nasa.gov

⁽¹³⁾Jet Propulsion Laboratory, California Institute of Technology, Pasadena, CA, 91109, USA. M/S 321-400.
adam.d.steltzner@jpl.nasa.gov

ABSTRACT

The Mars 2020 mission will land a rover on the surface of Mars that will acquire, encapsulate, and cache scientifically selected samples of martian material for possible return to Earth by a future mission. The samples will be individually encapsulated and sealed in sample tubes. Each sample, and therefore each sample tube, must be kept clean of viable organisms with a terrestrial origin, which may adhere to the rover on their own and/or on other non-biological particles. Therefore, contrary to previous missions to the Red Planet, Mars 2020 is subject to new and more stringent biological, organic and inorganic contamination requirements. This paper reports on the analyses and testing performed to assess the various vectors that can lead to the terrestrial-borne contamination of the samples, focusing on those that are predicted to be the larger contributors. Specifically, the contamination of the sample tubes is expected to be very small prior to the commencement of the mission's science phase since these tubes are protected by so-called Fluid Mechanical Particle Barriers. Once on the surface of Mars however the sample tubes will be removed from their FMPBs and be subject to contamination from the rover. Of specific interest is the vector by which winds

dislodge some particles from the surface of the rover and transport them to the surrounding soil. Naturally, such assessments require multi-disciplinary analyses involving at minimum the physics of particle adhesion and resuspension from surfaces, fluid mechanics and aerosols. Here we provide an overview of these models. We also report on particle resuspension experiments we have performed at the Jet Propulsion Laboratory to both guide and validate the aforementioned physics models.

1. INTRODUCTION

The Mars 2020 rover mission is part of NASA's Mars Exploration Program, a long-term effort of robotic exploration of the Red Planet. The primary science goals of the mission are as follows: (1) to characterize the processes that formed and modified the geologic record within a field exploration area on Mars selected for evidence of an astrobiologically relevant ancient environment and geologic diversity, (2) to perform specific astrobiologically relevant investigations on the geologic materials at the landing site and (3) to assemble rigorously documented and returnable cached samples for possible future return to Earth. Mars 2020 will leverage the proven design and technology developed for

the 2011 Mars Science Laboratory (MSL) mission that landed the Curiosity rover on Mars in August 2012 [1, 2]. Contrary to MSL however, the Mars 2020 rover will also acquire, encapsulate, and cache scientifically selected samples of martian material for possible return to Earth by a future mission. Therefore, parts of the mission that are associated with the samples are subject to new and more stringent biological, organic and inorganic contamination requirements compared to MSL. For example, the Level-1 requirement on biological contamination is that less than 1 Earth-sourced Viable Organism (VO) may be present in any deposited sample. The Level-2 requirement is that the probability of an Earth-sourced VO is less than 1 in 1000. “VO” here is the terminology we use to describe spores and other microbial organisms that could have the ability to reproduce under the appropriate environmental conditions.

To meet these requirements the Mars 2020 Project has developed over the last few years physics-based models of all known vectors that can lead to the contamination of the samples by terrestrial particles on the spacecraft, upon recognition that such particles can carry biological signatures. The development and validation of these models have been supported by laboratory tests. The models, in turn, are used to guide technology development and/or hardware cleaning that will allow us to meet these requirements, with ample margin. The most complex vectors are associated with the release and transport of particles by induced and/or ambient wind loads. Mechanical loads, such as those experienced by the vehicle during descent through the Mars atmosphere, can also release particles from the rover that remained adhered to the spacecraft during the previous phases of the mission. This article reports on a representative cross-section of the analyses and laboratory testing performed over the last few years to assess these more complex biological contamination vectors on Mars 2020.

1.1. Mission Timeline

Mars 2020 consists of a single spacecraft that will be assembled and tested primarily at the Jet Propulsion Laboratory (JPL). Upon completion of the Assembly, Test and Launch Operations (ATLO) the spacecraft will be launched from the Cape Canaveral Air Force Station or the Kennedy Space Center (KSC) in the summer of 2020 on an MSL-class launch vehicle. After separation from the launch vehicle, the spacecraft will begin a ~7-month cruise phase to Mars, with arrival in February 2021, depending upon the selected landing site. During cruise, the rover payload will be totally enclosed in an aeroshell. Like MSL and previous landed missions before that, the cruise stage will separate from the entry, descent and landing (EDL) system just prior to atmospheric entry, and follow an uncontrolled plunge through the martian atmosphere. The remaining portion of the spacecraft system will initiate a controlled direct EDL

sequence of activities. Upon rover touchdown, commissioning and science surface operations will be initiated. An illustration of the four major mission phases is shown in Fig 1. The prime mission duration is 1½ Mars years.



Fig 1. Mars 2020 timeline depicting the four major phases of the mission.

1.2. Critical Hardware and Biological Contamination Considerations Prior to Launch

A substantial portion of the Mars 2020 rover subsystems will be based on those of Curiosity with the exception of the new payload and the Sample Caching System (SCS), which contains (among others) the Adaptive Caching Assembly (ACA). The ACA is the collective set of hardware through which acquired samples will be inspected, encapsulated, and dropped on the surface of Mars. Several critical components of the ACA are depicted in in Fig 2. The assembly houses the sample tubes within the Sample Tube Storage (STS) assembly, Seals within the Seal Dispenser Assemblies, the Sample Handling Assembly, the Volume Assessment Station, the Vision Assessment Station, the tube warming station, Sealing/Sample Tube Drop-off Station, and the Bit Carousel, which contains 5 coring bits, 1 regolith bit and 2 abrading bits. Upon landing, the vent on the top deck and the belly pan covering the ACA will be deployed and the doors on the Bit Carousel will be opened. The sample tubes, volume probes and sealing plugs are all contained behind individual Fluid Mechanical Particle Barriers (FMPB).

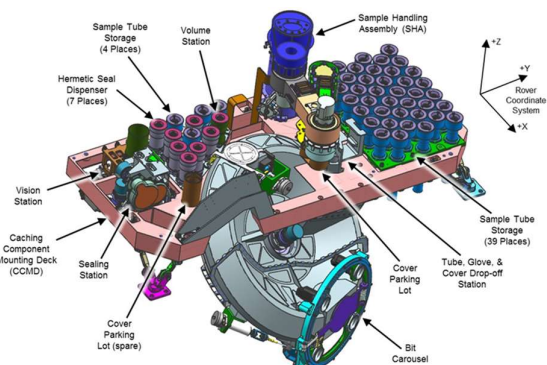


Fig 2. A detailed depiction of the Adaptive Caching Assembly.

An FMPB leverages fluid mechanical principles to prevent the transfer of particles from inside or outside the ACA during all mission phases, prior to the removal of

the sample tubes for sample acquisition. The first-principles behind its operation, along with results from computational fluid dynamics (CFD) simulations and Mars-similar flow experiments, have been reported elsewhere [3] and will therefore not be repeated here. For completeness however we mention that the work has shown particles as small as $0.15\ \mu\text{m}$ in diameter cannot penetrate deep enough to contaminate the sample tubes, under expected nominal [4] and off-nominal conditions on Mars such as dust devils.

Prior to system integration hardware will be cleaned to different levels, in stages, depending on the contamination risk they pose to the sample. To this end we have defined hardware that comes in direct contact with the sample as Sample Intimate Hardware (SIH). These include for example the Sample Tubes and (drill) Bit Assemblies. Hardware that comes into close proximity to the sample, or in direct contact or close proximity to SIH, is defined as Sample Handling Hardware (SHH). This category includes the Sample Tube Storage Assembly (STSA), Bit Carousel, and Vision Assessment Station for example. Contamination vectors associated with SIH and some SHH pose the highest risk and will therefore undergo the stringiest cleaning, which includes Dry Heat Microbial Reduction (DHMR) and in some cases firing in air at $350\ ^\circ\text{C}$. Such stringent cleaning methods are expected to reduce the NASA Standard Assay (NSA) spore bioburden by 4-12 orders of magnitude. Surfaces that are not part of SIH or SHH will be cleaned to less stringent levels using standard detergent/solvent immersion, sonication and rinse-based approaches. Similar processes were used also for MSL. In the remainder of this article we shall refer to such surfaces as having been “coarse-cleaned.”

2. MODEL DEVELOPMENT AND EXPERIMENTS IN SUPPORT OF THE SAMPLE CONTAMINATION ASSESSMENTS

A particle that remains adhered to the Mars 2020 rover after the surfaces have been cleaned will be liberated if the sum of one or more forces on it is large enough to overcome the particle-surface adhesion forces. We note here that a “particle” can be either biological, non-biological or a combination of the two. The release of these particles during the mission can lead to the biological contamination of the samples and is the focus of this article. Of course, processes other than particle resuspension and transport also may impact sample contamination. Microbial mortality due to long presence in vacuum and/or due to ultraviolet radiation on Mars are two examples. Such processes are accounted for in our final contamination tally but their assessment is beyond the scope of this article.

The two dominant loads on particles that can lead to their liberation on Mars are (1) gravitational acceleration and (2) aerodynamic loads. In most cases, aerodynamic loads on the particles will dominate. The release, or as it is most commonly termed by the aerosol community, the

“resuspension” phenomenon whereby particles adhering on a surface can be re-entrained by a flowing fluid is an area that has been investigated for several decades (the reader is referred to the excellent review article by Henry & Minier [5] for example). In this section we report on how lessons learned from the extensive work that has been performed in this rich subfield of aerosols, have helped facilitate the development of physics-based models and the design of laboratory experiments, to support the assessment of sample contamination on the Mars 2020 mission.

2.1. Physics Models and Simulations

A three-dimensional (3-D) numerical simulation code has been developed to facilitate the assessment of biological contamination of the samples. Because it brings together particle resuspension and transport physics models we have dubbed it the 3-D Particle Resuspension and Transport (PaRT3D) code. Its structure, capabilities and physics models are the subject of this section. PaRT3D is written in Fortran 90.

At present the code uses a finite-element model of the Mars 2020 rover but in principle it can accept any other discretized structure. Upon initialization of the rover geometry, the simulation proceeds with calculations according to the sequence of the various mission phases: ATLO, Cruise, EDL and Surface Operations, as shown in the basic flowchart in Fig 3-left. During each phase the particle distribution on the rover is exposed to different environments that can alter it. A typical result of the computed particle surface density around the spacecraft is provided in Fig 3-right. The ensuing sections describe in more detail the physics modules that contribute to the typical simulation result of Fig 3-right.

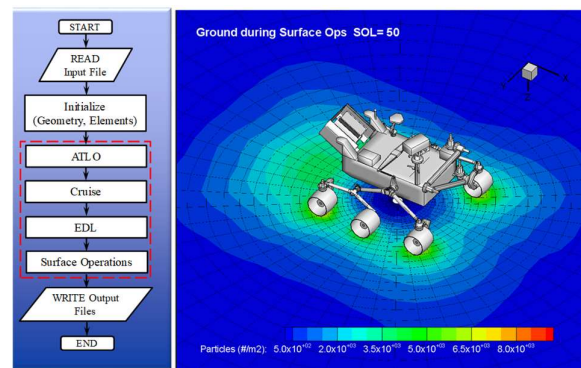


Fig 3. Left: High-level flowchart of the 3-D Particle Resuspension and Transport (PaRT3D) code, developed for the assessment of biological contamination of the samples on the Mars 2020 mission. Right: Typical output showing contours of particle surface density around the rover after 50 sols.

2.1.1. Initial particle distribution on the rover

In this section we describe the models that allow us to specify both biological and non-biological particle distributions on the majority of the rover surfaces. Here, by “majority of the rover” we refer to those surfaces that

have been coarse-cleaned. The more stringent cleaning of SIH and SHH will yield significantly different biological particle distributions and are beyond the scope of this article.

2.1.1.1. Non-biological particles. Recent measurements performed for Mars 2020 have shown that a large portion of the biological particles on the rover in ATLO will reside on non-biological particles. Therefore, any analyses that aims at determining biological contamination due to dislodgment of particles from the rover requires knowledge of the initial concentration of the non-biological particles on its surfaces. For surfaces that have only been coarse-cleaned we assume the distribution follows the military standard MIL-STD-1246C model for molecular cleanliness levels [6]:

$$N(d_p) = \alpha 10^{\beta(\log_{10}^2 CL - \log_{10}^2 d_p)} \quad (1)$$

where the coefficients are $\alpha=10.764$ and $\beta=0.926$. Equation (1) yields a cumulative distribution, that is, $N(d_p)$ is the number of particles per square meter (p/m^2) for particle diameter $\geq d_p$ (in microns, μm).

2.1.1.2. Biological particles. Since we are interested in biological contamination of the samples, the analyses also requires the number of VOs that are attached to non-biological particles and of those that are standalone. This information has been acquired by fallout measurements made in the Descent Stage (DS) and Spacecraft Assembly Facility (SAF) at JPL. DS and SAF are cleanrooms that fall under the International Organization for Standardization (ISO) class of ISO5 and ISO7, respectively.

The biogenic contamination was detected using an epifluorescence and Field Emission Scanning Electron Microscopy coupled with energy dispersive X-ray analysis. The measurements were binned in 11 different particle size ranges, from 0-1.9 μm to $>500 \mu m$, and were used to produce models for the VO/particle ratio. The model results and the data are plotted in Fig 4 as a function of the average particle diameter. The measurements showed no microbial organisms in particle diameter bins equal to or larger than 50-100 μm . It is not yet clear if the absence of microorganisms is simply the result of poor statistics due to the inherently low number of particles in these larger-size bins or if other processes were responsible. Thus, three models are considered in the analyses, denoted FO1, FO2 and FO3 in Fig 4. Currently, the simulations employ FO1 because it yields the most conservative results. When any of the FO models is applied in a calculation the values in Fig 4 are multiplied by a scale factor of ~ 0.5 to ensure that the total ATLO bioburden level is 600 spores/ m^2 assuming a ratio of VO to NSA spores (VO/spore) of 12,000.

2.1.2. Particle resuspension

The most dominant loads particles residing on the rover will experience during the mission will be due to aerodynamic forces and/or gravitational acceleration. In this section we describe the models we have developed to estimate (1) the minimum loads needed to initiate particle motion on the surface and (2) the fractions of the particles that are released upon application of the load. The particle size range that is of most relevance to our contamination assessments is 0.15-500 μm .

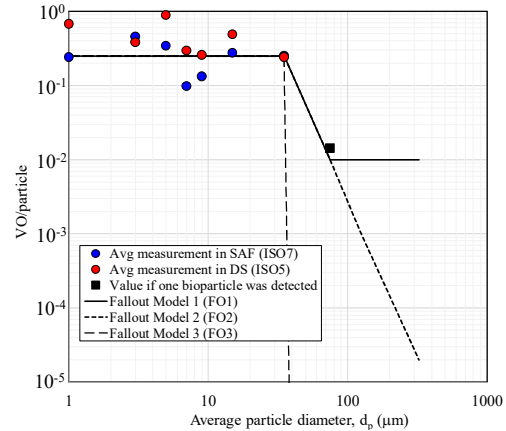


Fig 4. Three models (lines) of VO/particle ratio, FO1-3, based on fallout measurements (symbols) made in ISO5- and ISO7-class cleanrooms.

2.1.2.1. Aerodynamically induced resuspension. The majority of particles of interest will, in most cases, be within the viscous boundary layer (BL) that will form over the various rover surfaces as ambient wind flows over them on Mars. Thus, it is necessary to resolve the shear flow inside the BL. To better illustrate our approach we consider the idealized scenario of flow over a flat plate. In the absence of any other objects in the vicinity of the plate, and for laminar incoming flow of speed u_∞ , the transition from laminar to turbulent BL over a smooth surface is dependent upon the Reynolds number, $Re_x = \rho_\infty u_\infty x / \mu_\infty$ where ρ_∞ and μ_∞ are the mass density and dynamic viscosity of the freestream flow. When the BL is turbulent a thin region near the wall is formed called the viscous sublayer wherein the shear stress is uniform and the velocity increases linearly with distance from the wall. A body diagram of a particle in such shear flow is depicted in Fig 5, where F_p is the adhesion (or pull-off) force. F_D and F_L are the aerodynamic drag and lift forces, respectively. F_F is the friction force, F_G is the gravity force, and a is the contact radius.

It is well documented that in most cases a weaker force is needed to liberate a particle when it is applied in a direction parallel to the surface compared to the normal direction ([5] and references therein). Moreover, particle rolling is typically easier to induce than sliding. We therefore assume that the weakest force required to release a particle is that associated with its tangential motion, and compute only the forces and moments that are due to aerodynamic-induced rolling, adhesion and

gravitation. When the first exceeds the sum of the last two, that is

$$1.74d_p F_D/2 + aF_L > a(F_p + F_G) \quad (2)$$

then we consider the particle liberated from the surface and subject to the transport by the freestream flow. The criterion for particle rolling in Eq (2) may also be expressed in terms of the moment balance around point O. The flow-induced resuspension calculation then depends on two critical quantities: the so-called “threshold velocity” and the particle removal fraction (PRF).

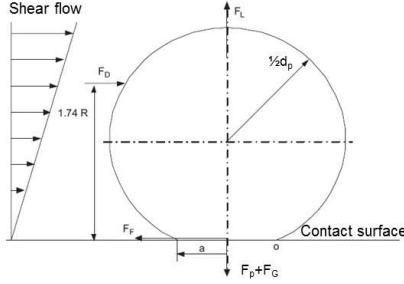


Fig 5. Forces on a particle adhered to a surface in shear flow.

(a) Determination of the threshold velocity.

The threshold velocity, u_T , is defined as the freestream velocity at which $PRF=0.5$. The model developed for its determination is based on the approach followed by Ibrahim, et al. [7]. F_p is determined by first computing the smooth-surface force, $F_{p0} = \varepsilon\pi\gamma d_p$, based on the Johnson-Kendall-Roberts (JKR) theory [8]. Here ε is a factor (between 1-2 for spherical particles) and γ is the surface energy (in J/m^2). To account for surface roughness F_{p0} is multiplied by C , a function of the surface asperity statistics and is always ≤ 1 . The model to determine C is based on the formulations of Cheng, et al. [9]. The statistics of the surface asperities are an input to the model, and is determined by direct measurement. The (rough-surface) pull-off moment M_p can then be determined as follows:

$$M_p = aCF_{p0}. \quad (3)$$

The contact radius is obtained from the JKR theory, which requires knowledge of the combined Young's modulus and Poisson's ratio for both the particle and the surface on which it resides [7].

The lateral hydrodynamic force on the particle in the shear layer is Stokes drag multiplied by the correction factors C_{Kn} and C_{Re} as given by Eq. (4) to account for slip and Reynolds number effects, respectively. They are empirically derived functions of the particle Knudsen and Reynolds numbers [10, 11].

$$F_D = 3\pi\mu_c d_p \frac{C_{Re}}{C_{Kn}} \quad (4)$$

It is convenient to define the non-dimensional parameters $u^+ \equiv u_c/u_*$ and $y^+ \equiv u_* d_p/2\mu_\infty$ where u_c is the flow speed at a

height equal to the distance from the centre of the (spherical) particle to the surface. We also define the so-called friction velocity: $u_* \equiv (\tau_w/\rho_\infty)^{1/2}$ with τ_w denoting the shear stress at the wall. Surface effects inside the viscous sublayer due to the presence of a particle are taken into account by the O'Neil factor, $f=1.7009$ [12]. In the viscous sublayer it is known that $u^+=y^+$ for a smooth surface. But it has also been argued that particle resuspension may be enhanced by burst sweeps of turbulence. These effects are taken into account in the resuspension model based on the work of Soltani, et al. [13], which provides a non-linear dependence of u^+ on y^+ . With knowledge of $u^+=f(y^+)$ and u_* , u_c can be determined and, ultimately, the drag rolling moment $M_D = M_o(F_D)$:

$$M_D = 1.74d_p F_D/2. \quad (5)$$

Once the drag force and rolling moment have been determined, the “threshold” velocity u_T is then obtained as the freestream value at which, $M_p + M_g = M_D$, where $M_g \equiv \rho_p V_p a g$, with ρ_p and V_p being the mass density and volume of the particle, respectively.

(b) Determination of the particle removal fraction.

The threshold velocity is used in the second sub-model to obtain the PRF. The model assumes a cumulative distribution function with lognormal distribution for the velocity as given by Eq (6). The standard deviation σ is associated with the relative surface roughness and is assumed to scale linearly with the particle diameter d_p : $\sigma = \sigma_0 d_p/d_{p0}$. In Eq (6), $\bar{u} = u_\infty/u_T$.

$$PRF(u_\infty, u_T) = \frac{c}{\sqrt{2\pi}} \int_{-\infty}^{\log_{10}(\bar{u})/\sigma} e^{-t^2} dt \quad (6)$$

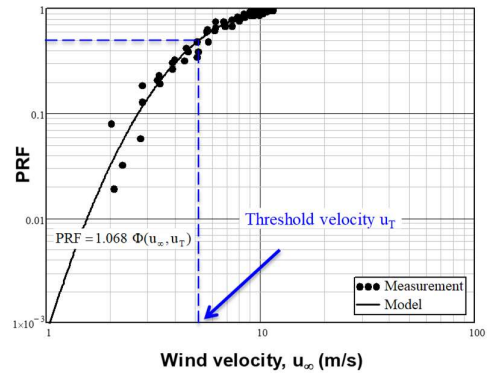


Fig 6. Comparison between the computed and measured PRFs of 70- μ m glass particles on a glass surface. The data is taken from [14].

Published PRFs for GoG resuspension obtained in the wind tunnel experiments of Ibrahim, et al. [7, 14] have been used to validate the model. Specifically, using the PRF measurements for $d_p=70 \mu$ m as the reference, we find that the PRF indeed follows closely the lognormal distribution, with a value of the coefficient $c=1.07$, as

shown in the comparison of Fig 6. When the model is applied to $d_p=30 \mu\text{m}$, and using the scaling of the standard deviation in Eq. (6), we find $c=0.993$. Considering that for both particle sizes the deviation from the lognormal distribution is $<10\%$, we assume in our resuspension calculations that $c=1$.

The computed PRFs for particle diameters 25-200 μm are plotted in Fig 7 as a function of flow speed on Mars based on the GoG PRF model. Also plotted for reference are the expected mean (4.7 m/s) and 99-th percentile (15.3 m/s) wind speeds under nominal conditions on the surface of Mars [4], along with the expected maximum speed the rover will experience at heat shield separation (~ 167 m/s). The results on Fig 7 assumed an atmospheric mass density of $2.2 \times 10^{-2} \text{ kg/m}^3$.

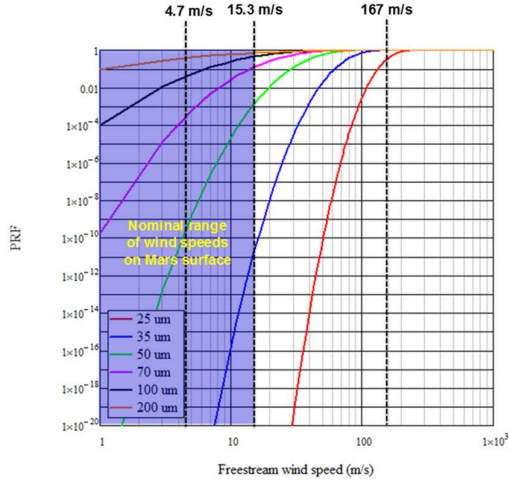


Fig 7. Resuspension by aerodynamic loads: Particle removal fraction (PRF) as a function of freestream wind speed on Mars for different particle diameters.

In addition to a model for σ , determination of the PRF requires knowledge of u_T , which in turn requires knowledge of u_* . In principle, u_* may be determined either by direct measurement (as in [14]), numerical simulation, or in idealized cases by analytical means from thin BL theory. In PaRT3D the latter is the default option. Specifically, in a simulation each rover element is considered to be a flat plate from the viewpoint of a particle that resides on it. This allows us to employ the well-established semi-empirical relation for the friction coefficient c_{fT} associated with a turbulent boundary layer (TBL) over a flat plate:

$$c_{fT} \equiv \frac{2\tau_w}{\rho_\infty u_\infty^2} = 2 \left(\frac{u_*}{u_\infty} \right)^2 = \frac{0.0594}{\text{Re}_x^{1/5}} \quad (7)$$

The distance from the leading edge, x , is an input to the model. Several CFD simulations have been performed to evaluate the fidelity of the flat-plate TBL model and to guide the choice of x in Eq (7). Fig 8 compares the number of particles released from the rover when τ_w was determined directly from CFD Reynolds Averaged Navier Stokes (RANS) simulations of flow

over the rover, with the number computed using two versions of the idealized model in Eq (7). In first model termed ‘‘Flat Plate TBL (u_∞, x)’’ we assumed each rover element is a flat plate that experiences a tangential flow speed equal to the freestream velocity, u_∞ . In the results of Fig 8 $u_\infty=15.3 \text{ m/s}$ in Eq (7). In the second model, termed ‘‘Flat Plate TBL ($2u_\infty \text{Rand}[0:1], x=0.5\text{cm}$),’’ the tangential velocity was applied randomly over the rover elements (with a uniform distribution between 0-1) and was limited to a wind speed $< 2u_\infty$. Here, $\text{Rand}[0:1]$ denotes random numbers between 0-1 that are generated based on a uniform probability density distribution. The sensitivity of the results on two values of x were assessed, $x=0.5$ and 1 cm, as plotted in Fig 8. To evaluate the sensitivity of the numerical results, we performed CFD simulations from a matrix of cases that combined different RANS turbulence closure models and wind directions as follows. We employed two turbulence models, Menter’s Shear Stress Transport (SST) $k-\omega$ and the Standard $k-\epsilon$, and assessed three different flow directions: tailwind, headwind and crossflow. Representative results for headwind using the (SST) $k-\omega$ model are shown in the contoured plot of Fig 9. All CFD simulations accounted for the atmospheric boundary layer by specifying a variation in the freestream velocity as a function of distance from the ground, z .

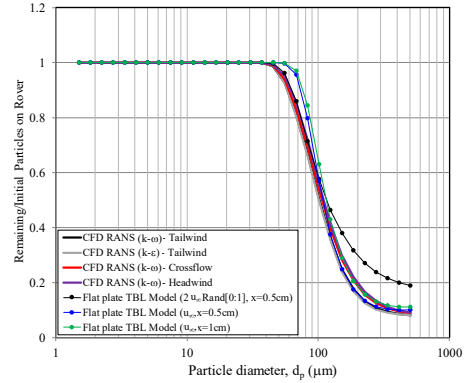


Fig 8. Comparison of particle removal from the rover using shear stresses from CFD RANS simulations and those from the idealized model of a TBL over a flat plate in PaRT3D (Eq (7)).

The comparisons in Fig 8 for the ratio of remaining/initial number of particles on the rover show small differences between the various CFD solutions. Compared to the Flat Plate TBL model solutions, we find the largest differences to be with the solution that dispersed randomly the shear stress on the rover. Compared to the Flat Plate TBL model with fixed velocity over the elements, the discrepancy with the CFD solution is 11-17% for $70 \leq d_p \leq 100 \mu\text{m}$ and 14-20% for $415 \leq d_p \leq 510 \mu\text{m}$; for all other particle sizes it is below 10%. Because the contamination associated with particles in the size range of $70 \leq d_p \leq 100 \mu\text{m}$ is expected to be higher, we use this Flat Plate TBL model with fixed velocity u_∞ and $x=0.5 \text{ cm}$, as our baseline.

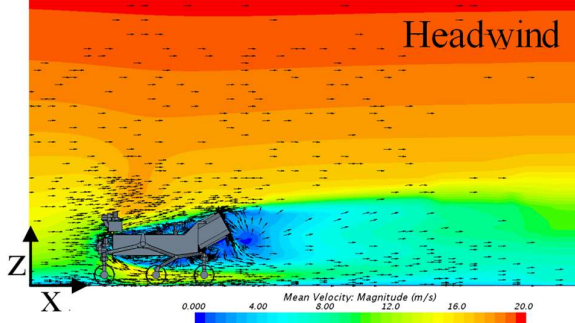


Fig 9. Results from CFD RANS simulations showing flow speed contours and velocity field over the rover.

2.1.2.2. Resuspension induced by mechanical loads

The most commonly used diagnostic to measure the removal of particles from a surface upon application of gravitational acceleration is a centrifuge (CFG). As it will be shown with more detail in Sec 2.2.3, PRF measurements with a CFG yield wide-ranging results that make the development of a model challenging at best and ambiguous at worst. Consequently, to obtain the fraction of particles removed by mechanical loads we use the aerodynamics models developed and validated with tests for flow-induced particle resuspension, as discussed in Sec 2.1.2.2. Specifically, given an applied g -load we compute the tangential force associated with it and use the flow-induced model to determine the mechanically-induced PRF. The approach is supported by experiments we performed with two CFGs and is discussed with more detail in Sec 2.2.3.

2.1.3. Particle Transport

Once a particle is released from a rover surface, a separate tracking algorithm is employed in a PaRT3D simulation to determine its trajectory. The aerodynamic force applied to the liberated particle was given by Eq (4) with the exception that $f=1$ and u_c is now the freestream velocity u_∞ . Integration of the equation of motion for a particle in fixed flow and gravitational fields of velocity $\mathbf{u}(u_x, u_y, u_z)$ and acceleration $\mathbf{g}=g\hat{z}$ respectively, yields the position vector $\mathbf{r}(t, x, y, z)$ in the Cartesian coordinate system as follows:

$$x(t) = x_0 + u_x t + \left(\frac{\dot{x}_0 - u_x}{k_p} \right) (1 - e^{-k_p t}) \quad (8a)$$

$$y(t) = y_0 + u_y t + \left(\frac{\dot{y}_0 - u_y}{k_p} \right) (1 - e^{-k_p t}) \quad (9b)$$

$$z(t) = z_0 + (u_z - u_{Tp})t + \left(\frac{\dot{z}_0 - u_z + u_{Tp}}{k_p} \right) (1 - e^{-k_p t}) \quad (9c)$$

where subscript “0” denotes the initial condition for the particle. Also, $\dot{\mathbf{r}}=\mathbf{u}_p$, ρ_p is the mass density of the particle,

$k_p=g/u_{Tp}$ and u_{Tp} is the terminal velocity of the particle.

In a typical PaRT3D simulation we first determine the reduction of particles (both non-biological and biological) from each rover element. The trajectories of “macro-particles” in a given diameter bin, each representing the surface density of particles on the rover element from which they were released, is then determined using Eqs (9). This calculation allows us to determine the landing locations of these particles on a domain around the rover that represents the surface of Mars. In a simulation this domain is discretized using a computational mesh that is comprised of quadrilateral elements. An example of the computed particle surface density in the vicinity of the rover was shown in Fig 3. This simulation was produced by applying an aerodynamic load on each rover element that was randomly distributed in all directions ($0-2\pi$) of the x - y plane. A random generator between 0-1 with uniform probability density distribution was used for both the magnitude and direction of the velocity field. The load on the released particles was due to an average wind speed of 4.7 m/s, assumed to occur every solar day (sol) on the surface of Mars for 50 sols. This calculation, as well as all others associated with Mars surface operations, do not take into account obstruction of a given particle trajectory from a rover element due to the presence of another object on the rover. The resulting ground contamination therefore overestimates in general the true contamination on the surface of Mars.

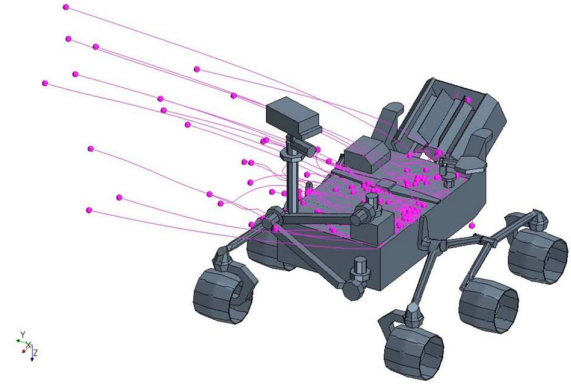


Fig 10. Trajectories of 100- μm particles computed using a Lagrangian particle tracker and LES of a 15.3-m/s crossflow.

A natural question that arises from the application of a randomly distributed velocity field over the rover is how more accurate would the computed contamination be if the real flow field over the rover was accounted for? In addition to the RANS simulations, we have therefore also performed a few representative Large Eddy Simulations (LES) and combined them with a Lagrangian particle tracker (in the same CFD simulation) to determine the particle trajectories and landing locations. The LES were performed for three different scenarios: (i) 15.3-m/s tailwind, (ii) 15.3-m/s crossflow and (iii) 4.7-m/s headwind. For all three cases, we

compared the landing locations of 100- μm and 500- μm particles. The particle trajectories in PaRT3D were computed using Eqs (9) assuming a randomly distributed flow field, with a mean speed that varied 14-15 m/s. Typical trajectories of 122 particles soon after they were launched from the rover in the LES (case ii) are shown in Fig 10. All particles in these simulations were initially located on the main rover deck. These comparisons showed qualitatively similar results and allowed us to quantify our uncertainties in the PaRT3D approach.

2.2. Laboratory Experiments

2.2.1. Rover surface roughness measurements

It is well known that the roughness of the surfaces associated with the particle and material to which it adheres can have a significant effect on the resuspension rates ([5, 14] and references therein). We have therefore measured the roughness of four materials that are most abundant on the rover: two types of white paint, anodized aluminium and kapton. Because some of our model validation tests involved particles on glass substrates we have also measured the asperity statistics of glass. The measurements were performed by Atomic Force Microscopy (AFM). Each coupon was scanned in $1 \times 1 \mu\text{m}^2$ and $5 \times 5 \mu\text{m}^2$ areas. One example of an AFM image is shown in Fig 11, for S-13 white paint. The average surface roughness, R_a (in μm), from these measurements is listed for each material in Table 1. These measurements can be used directly in our resuspension models as input (through the function C in Eq (3)).

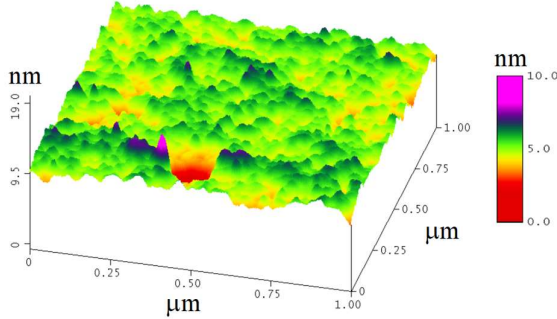


Fig 11. Images from AFM measurements of the surface roughness of S-13 white paint.

Table 1. Average surface roughness (R_a) measurements for different materials, obtained with an AFM.

Material	R_a (μm)
White paint (S-13)	6.48
White paint (Aptek 2711)	2.06
Anodized Aluminum (6061)	0.64
Kapton polyimide	0.1
Glass	0.04

2.2.2. Aerodynamically induced resuspension

2.2.2.1. Experimental Approach. Numerous flow experiments that produced PRF measurements are reported in the literature, most of which employed a wind tunnel (e.g. see Henry & Minier [5] and references therein). In our laboratory investigations we have used a Laminar Flow Device (LFD) similar to the one designed and used by Phares, et al. [15]. The device consists mainly of a small high-aspect-ratio rectangular channel, which makes it highly portable. Perhaps the most suitable feature of the device however is that the shear stress at the walls (where the particles reside) is a well-known function of the flow rate and geometry of the device:

$$\tau_w = \mu \left. \frac{\partial u}{\partial y} \right|_{y=\pm d} = \frac{6Q\mu}{H^2W} \quad (9)$$

where H and W are the channel height and width, respectively. The volumetric flow rate is Q . This allows for direct measurements of the PRF without additional measurements of the flow velocity inside the viscous BL.

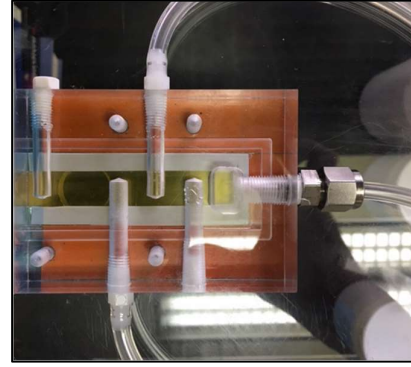


Fig 12. Photograph of the LFD used in the particle resuspension experiments.

A photograph of the acrylic version of the device is provided in Fig 12. A (non-transparent) metallic version of the device with identical dimensions (provided to us courtesy of R. Flagan, California Institute of Technology) was used successfully in the past in resuspension tests of polystyrene particles [15]. Air flow into the LFD is provided by a mass flow controller through the rectangular opening shown on the right in Fig 12. The test substrate is placed at the opposite end, under a viewing window to allow for the visualization of the particle surface density before and after the supply of the flow. The channel height was held to $380 \mu\text{m}$ using a Teflon shim placed between the substrate and the base of the device. The long channel and shim can be seen in the middle of Fig 12.

To obtain the PRF for any given pair of particle type and substrate, the flow rate was increased in successive increments over the range of 0.1-10 L/min (~ 0.5 -50 m/s). The pressure drop in the channel was monitored through a series of pressure ports located along the centreline of the channel (see Fig 12), using a differential pressure

gauge. At maximum flow rate (10 L/min) the Reynolds number (based on the channel height H) was almost 900. The friction velocity and walls shear stress were 2.6 m/s and 10.1 Pa, respectively. The particles were deposited by gravitational settling on thin slides of different materials. The target particle surface densities on the slides were under 50 p/cm² to reduce saltation effects [7, 14]. The slides were first cleaned using a detergent/nitric acid solution. Following cleaning, they were stored in an oven at 100 °C. For tests with idealized spherical particles we used 70 (± 5)- μm borosilicate glass and SS particles. For tests with non-idealized particles we used 40-80 μm Arizona Fine Dust (AFD). The PRFs were determined from sequential images acquired by a Keyence video microscope through the LFD’s 19-mm diameter viewing port (Fig 12).

To the best of our knowledge, PRF measurements for all combinations of dust on surfaces common to the Mars 2020 rover are not available. Therefore, prior to using the LFD to produce these new measurements, we performed a series of validation experiments with idealized particles and substrates. The objective was to compare our measurements with well-established data from the peer-reviewed literature. One of the most comprehensive and broadly cited studies of particle resuspension was performed by Ibrahim, et al. [7, 14], in which a wide range of parameters that could affect the resuspension rates was investigated through controlled experiments in a wind tunnel. We compared our measurements for stainless steel microspheres on glass in laminar flow and found the PRFs to be in good agreement.

2.2.2.2. Experiments with dust particles on rove-representative surfaces. The ultimate objective of the experiments discussed in this section was to determine the PRFs of dust particles liberated from materials that are most prominent on the Mars 2020 rover. We used the LFD to characterize the PRFs of AFD from kapton (DoK), anodized aluminum (DoA), S-13 white paint (DoWp) and glass (DoG). The experimental approach was the same as that used in the idealized tests described in the previous section.

The PRFs for DoG from several tests using 40-80 μm AFD particles are plotted in Fig 13. Also plotted is the average PRF from the tests with the LFD using 70 (± 5) μm glass microspheres. For all cases, the comparisons revealed that the aerodynamic shear stress required to liberate a fraction of glass particles from a glass surface is, in general, smaller or comparable to that required to liberate the same fraction of dust particles from all the surfaces we tested. We argue that the main reason behind the observed PRF trends is associated with effect of the relative roughness of the two surfaces on the particle motion prior to lift-off. To better illustrate how this particle motion along the surface may have been impeded in the AFD tests, we performed scanning electron microscopy (SEM) on a few representative particle-substrate pairs. An example is provided in Fig 14. The

images showed clearly that it would be much easier to roll and/or slide the spherical particles than the dust particles because the contact surfaces in the latter are dominated by highly non-symmetrical morphologies that impede lateral motion of the particle.

These findings have important implications on our contamination assessments because they allow us to use well-studied and validated resuspension models for GoG, rather than the less tractable models for dust, since the former will always yield larger or comparable removal fractions than the latter. Consequently, the contamination is also expected to be comparable or larger when the GoG PRFs are used than any other dust-surface combination. In this respect GoG resuspension can therefore be considered as yielding the most conservative contamination results.

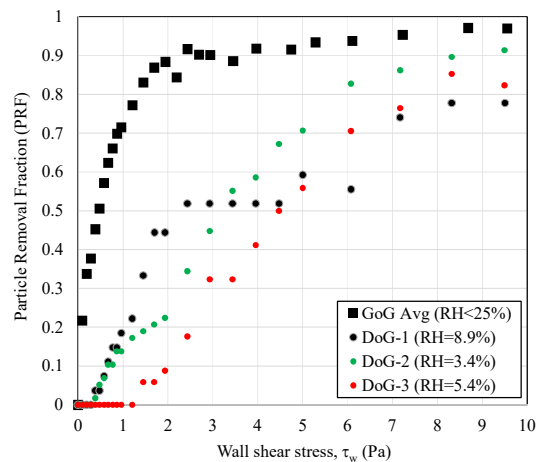


Fig 13. The measured PRFs from several resuspension tests with the LFD, comparing measured PRFs for DoG with the average PRF from GoG data.

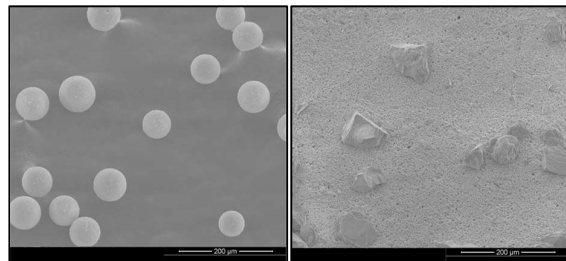


Fig 14. Images of spherical and (non-spherical) dust particles on surfaces taken with a SEM. Left: 70- μm glass microspheres on carbon tape. Right: 40-80 μm AFD on (S-13) white paint.

2.2.3. Mechanically induced resuspension

It has been well documented in the literature that tests with a CFG - the most commonly used instrument for the measurement of PRFs as a function of applied (g) acceleration - yield removal fractions that can vary over a very wide range at each specific g -load (e.g. see [16]). We have reproduced this behaviour, using two different CFGs and particles with size that ranged 8-80 μm . The particle deposition, substrate cleaning and coupon

storage methods were the same as those used in the LFD tests. An example of PRF measurements for GoG resuspension with 70 (± 5)- μm particles obtained from a series of five different tests are presented in Fig 15. With such wide-ranging statistics in the CFG measurements, it is impossible to develop and validate a deterministic physics-based model of the PRF as a function of applied acceleration. Though semi-empirical models can be (and have been) developed [16], they are associated with an uncertainty that is prohibitively large for our mission contamination assessments. We argue that the mechanics of overcoming the adhesion force are similar when a laminar aerodynamic force and when a gravitational force are applied on the particle in the tangential direction. We proceeded therefore to extract the applied tangential force from the LFD and CFG experiments. The results for the 70 (± 5)- μm GoG tests are compared in Fig 15. The comparison clearly shows that the variability in the PRF values at a given applied force is much smaller in the flow tests than it is in the CFG tests. Furthermore, the flow test values appear to set the upper bound for the PRF since almost all CFG data reside within or below the range of the flow test data.

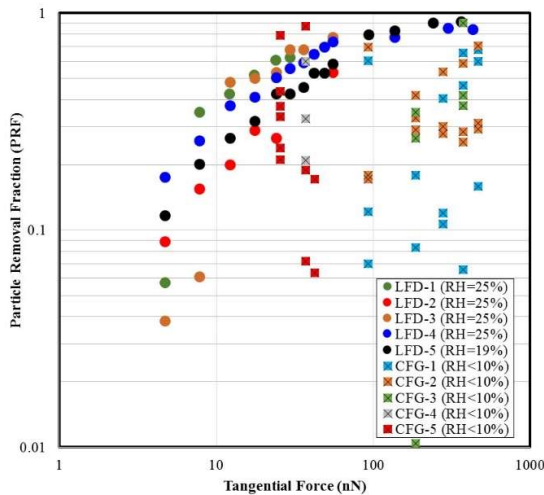


Fig 15. Measured GoG PRFs for 70 (± 5)- μm particles comparing results obtained with the LFD and CFG.

3. ACKNOWLEDGMENT

The research described in this paper was carried out by the Jet Propulsion Laboratory, California Institute of Technology, under a contract with the National Aeronautics and Space Administration. The authors would like to extend their gratitude to Dr. A. H. Ibrahim Essawey (Cairo University) for providing some of the GoG and SSoG PRF data, and Prof. Richard Flagan (California Institute of Technology) for his support and for making available the metallic version of the LFD.

4. REFERENCES

[1] J. J. Wray, "Gale crater: the Mars Science Laboratory/Curiosity Rover Landing Site," *International Journal of Astrobiology*, vol. 12, no. 1, pp. 25-38, Jan, 2013.

[2] D. F. Blake, et al., "Curiosity at Gale Crater, Mars: Characterization and Analysis of the Rocknest Sand Shadow," *Science*, vol. 341, no. 6153, Sep 27, 2013.

[3] I. G. Mikellides, et al., "The viscous Fluid Mechanical Particle Barrier for the prevention of sample contamination on the Mars 2020 mission," *Planetary and Space Science*, vol. 142, pp. 53-68, Aug, 2017.

[4] J. R. Murphy, C. B. Leovy, and J. E. Tillman, "Observations of Martian Surface Winds at the Viking Lander-1 Site," *Journal of Geophysical Research-Solid Earth and Planets*, vol. 95, no. B9, pp. 14555-14576, Aug 30, 1990.

[5] C. Henry, and J. P. Minier, "Progress in particle resuspension from rough surfaces by turbulent flows," *Progress in Energy and Combustion Science*, vol. 45, pp. 1-53, Dec, 2014.

[6] *MIL-STD-1246C, Military Standard: Product Cleanliness Levels Contamination Control Program.*

[7] A. H. Ibrahim, P. F. Dunn, and M. F. Qazi, "Experiments and validation of a model for microparticle detachment from a surface by turbulent air flow," *Journal of Aerosol Science*, vol. 39, no. 8, pp. 645-656, Aug, 2008.

[8] K. L. Johnson, K. Kendall, and A. D. Roberts, "Surface Energy and Contact of Elastic Solids," *Proceedings of the Royal Society of London Series a-Mathematical and Physical Sciences*, vol. 324, no. 1558, pp. 301-&, 1971.

[9] W. Cheng, P. F. Dunn, and R. M. Brach, "Surface roughness effects on microparticle adhesion," *The Journal of Adhesion*, vol. 78, no. 11, pp. 929-965, 2002/11/01, 2002.

[10] D. J. Rader, "Momentum Slip Correction Factor for Small Particles in 9 Common Gases," *Journal of Aerosol Science*, vol. 21, no. 2, pp. 161-168, 1990.

[11] L. Schiller, and A. Naumann, "Fundamental calculations in gravitational processing," *Zeitschrift Des Vereines Deutscher Ingenieure*, vol. 77, pp. 318-320, 1933.

[12] M. E. O'Neill, "A Sphere in Contact with a Plane Wall in a Slow Linear Shear Flow," *Chemical Engineering Science*, vol. 23, no. 11, pp. 1293-&, 1968.

[13] M. Soltani, and G. Ahmadi, "Direct Numerical-Simulation of Particle Entrainment in Turbulent Channel Flow," *Physics of Fluids*, vol. 7, no. 3, pp. 647-657, Mar, 1995.

[14] A. H. Ibrahim, "Microparticle detachment from surfaces by fluid flow," University of Notre Dame, 2004.

[15] D. J. Phares, G. T. Smedley, and R. C. Flagan, "Effect of particle size and material properties on aerodynamic resuspension from surfaces," *Journal of Aerosol Science*, vol. 31, no. 11, pp. 1335-1353, Nov, 2000.

[16] J. B. Barengoltz, "Particle Adhesion to Surfaces under Vacuum," *Journal of Spacecraft and Rockets*, vol. 26, no. 2, pp. 103-108, Mar-Apr, 1989.